

Skin-Integrated Devices with Soft, Holey Architectures for Wireless Physiological Monitoring, With Applications in the Neonatal Intensive Care Unit

Sung Soo Kwak, Seonggwang Yoo, Raudel Avila, Ha Uk Chung, Hyoyoung Jeong, Claire Liu, Jamie L. Vogl, Joohee Kim, Hong-Joon Yoon, Yoonseok Park, Hanjun Ryu, Geumbee Lee, Jihye Kim, Jahyun Koo, Yong Suk Oh, Sungbong Kim, Shuai Xu, Zichen Zhao, Zhaoqian Xie, Yonggang Huang,* and John A. Rogers*

Continuous monitoring of vital signs is an essential aspect of operations in neonatal and pediatric intensive care units (NICUs and PICUs), of particular importance to extremely premature and/or critically ill patients. Current approaches require multiple sensors taped to the skin and connected via hard-wired interfaces to external data acquisition electronics. The adhesives can cause iatrogenic injuries to fragile, underdeveloped skin, and the wires can complicate even the most routine tasks in patient care. Here, materials strategies and design concepts are introduced that significantly improve these platforms through the use of optimized materials, open (i.e., “holey”) layouts and precurved designs. These schemes 1) reduce the stresses at the skin interface, 2) facilitate release of interfacial moisture from transepidermal water loss, 3) allow visual inspection of the skin for rashes or other forms of irritation, 4) enable triggered reduction of adhesion to reduce the probability for injuries that can result from device removal. A combination of systematic benchtop testing and computational modeling identifies the essential mechanisms and key considerations. Demonstrations on adult volunteers and on a neonate in an operating NICUs illustrate a broad range of capabilities in continuous, clinical-grade monitoring of conventional vital signs, and unconventional indicators of health status.

1. Introduction

Each year, more than 480 000 infants and children in the United States are admitted to intensive care units (ICUs). Those under 1 year of age, particularly very low-birth-weight premature infants, suffer from high rates of morbidity and mortality.^[1–3] For these fragile patients, real-time monitoring of their vital signs represents an essential aspect of care. Traditional systems for such purposes in the neonatal and pediatric ICUs (NICUs and PICUs) involve multiple electrodes and sensors that attach to various parts of the body using adhesive tapes. Hard wires form interconnections to external electronic processing and storage units. These platforms can provide high quality data but they have significant disadvantages. For neonates and pediatric patients with immature skin, iatrogenic injuries, and subsequent scarring can result from the electrodes/sensors and adhesives.^[4–6] This hardware also frustrates natural movements, it creates practical difficulties in

S. S. Kwak, S. Yoo, H. Jeong, C. Liu, J. Kim, H.-J. Yoon, Y. Park, H. Ryu, G. Lee, J. Kim, S. Xu, Y. Huang, J. A. Rogers
Querrey Simpson Institute for Bioelectronics
Northwestern University
Evanston, IL 60208, USA
E-mail: y-huang@northwestern.edu; jrogers@northwestern.edu

R. Avila, Y. Huang, J. A. Rogers
Department of Mechanical Engineering
Northwestern University
Evanston, IL 60208, USA

H. U. Chung, S. Xu
Sibel Health
Niles, IL 60714, USA

 The ORCID identification number(s) for the author(s) of this article can be found under <https://doi.org/10.1002/adma.202103974>.

DOI: 10.1002/adma.202103974

C. Liu, J. A. Rogers
Department of Biomedical Engineering
Northwestern University
Evanston, IL 60208, USA

J. L. Vogl
Division of Pediatric Autonomic Medicine
Department of Pediatrics
Ann & Robert H. Lurie Children's Hospital of Chicago
Chicago, IL 60611, USA

J. Koo
School of Biomedical Engineering
Korea University
Seoul 02841, Republic of Korea

J. Koo
Interdisciplinary Program in Precision Public Health
Korea University
Seoul 02841, Republic of Korea

feeding, changing diapers and bathing, and it limits opportunities for physical bonding with parents through skin-to-skin contact (i.e., kangaroo care, KC).^[3]

Soft, wireless electronic devices can overcome these and other drawbacks of traditional monitoring equipment, to enable safe and effective care for vulnerable patients.^[7–16] Soft, flexible, and biocompatible hydrogels are options in skin-interfaces for integrated circuit systems designed for health monitoring.^[17] Two such types of technologies have been demonstrated with patients in NICU and PICU facilities.^[18,19] The most advanced systems operate in a battery-free manner, through devices that have ultrathin, stretchable, “skin-like” characteristics. A time-synchronized pair can capture heart rate (HR), heart rate variability (HRV), respiration rate (RR), blood oxygen saturation (SpO₂), pulse wave velocity, and skin temperature at the chest and at a limb, all with clinical-grade levels of accuracy. The thin, low modulus properties, and wireless operation of these devices allow robust bonding to the skin with interfacial adhesives that require bonding strengths that are more than ten times less

than those needed with conventional wired sensors, thereby reducing the probability for iatrogenic skin injuries during removal. Additional important features include sparse architectures that provide optical transparency, for visual inspection of the skin interface, and electromagnetic designs that allow use of magnetic resonance imaging and X-ray computed tomography, for various diagnostic purposes. A limitation of this technology is that the mechanical fragility of the devices leads to practical difficulties in multiple cycles of application, removal, and sterilization, particularly relevant for use in the home or in lower and middle income countries. Also, the near-field communication (NFC) schemes for wireless power delivery and communication require reliable wall-plug power, RF transmission hardware, and specialized electronics. Furthermore, the protocols can only support operating ranges and data transfer rates of up to 30 cm and a few hundred Hz, respectively. Related constraints prevent monitoring modalities that extend beyond the current clinical standard of care.^[18]

A second study introduced an alternative, complementary platform based on Bluetooth technology and small, rechargeable batteries, with capabilities that bypass these and other limitations of the NFC system.^[19] Advanced functional modes support capabilities in monitoring movements and changes in body orientation, in capturing seismocardiograms (SCGs) and in recording vocal biomarkers and other sounds of body functions (e.g., respiration, gastrointestinal processes, etc.), each of relevance for early detection of complications related to birth trauma, brain injury, and/or or pain stress.^[20,21] Relative to the NFC platforms, these systems have larger thicknesses, masses, and effective mechanical properties, they require stronger adhesives to maintain robust bonding to the skin, particularly at highly curved regions on the most premature babies,^[22] and they have an opaque construction that prevents optical inspection of the skin/device interface.

This paper introduces concepts that address these disadvantages through the use of optimized materials in open, or “holey,” device architectures and with precurved layouts. The holes, with strategic locations and dimensions defined by finite element analysis (FEA), enhance the flexibility and stretchability of the devices in various directions that are important to practical use. Perhaps more significantly, these features also provide multiple points of access for introducing warm water to the skin interface. The consequent swelling of hydrogel adhesives molded with microfluidic channel structures dramatically reduces the bonding strength, in some cases to negligible values, to facilitate device removal.^[23–25] Additional aspects of this design include 1) visual access to the underlying skin, for clinical inspection for irritation or allergic reactions, and 2) mechanisms for enhanced evaporation of water released through natural transepidermal mechanisms or sweating.^[26,27] Precurved shapes tailored to the match the surfaces of desired mounting locations minimize bending forces and corresponding stresses at the skin interface. Systematic studies of devices designed to monitor a full range of conventional and unconventional metrics of physiological health reveal all of the key aspects of these advanced materials and design ideas. Demonstrations on adult volunteer subjects and patients in an operating NICU illustrate the operational features in realistic settings.

Y. S. Oh

Department of Mechanical Engineering
Korea Advanced Institute of Science and Technology
Daejeon 34141, Republic of Korea

S. Kim

Department of Materials Science and Engineering
University of Illinois at Urbana Champaign
Urbana, IL 61801, USA

S. Xu

Department of Dermatology
Division of Dermatology
Department of Pediatrics
Feinberg School of Medicine
Northwestern University
Chicago, IL 60611, USA

Z. Zhao, Z. Xie

State Key Laboratory of Structural Analysis for Industrial Equipment
Department of Engineering Mechanics
Dalian University of Technology
Dalian 116024, China

Z. Zhao, Z. Xie

Ningbo Institute of Dalian University of Technology
Ningbo 315016, China

Y. Huang, J. A. Rogers

Department of Civil and Environmental Engineering
Northwestern University
Evanston, IL 60208, USA

Y. Huang

Department of Materials Science and Engineering
Northwestern University
Evanston, IL 60208, USA

J. A. Rogers

Department of Chemistry
Northwestern University
Evanston, IL 60208, USA

J. A. Rogers

Department of Neurological Surgery
Feinberg School of Medicine
Northwestern University
Chicago, IL 60611, USA

J. A. Rogers

Department of Electrical and Computer Engineering
Northwestern University
Evanston, IL 60208, USA

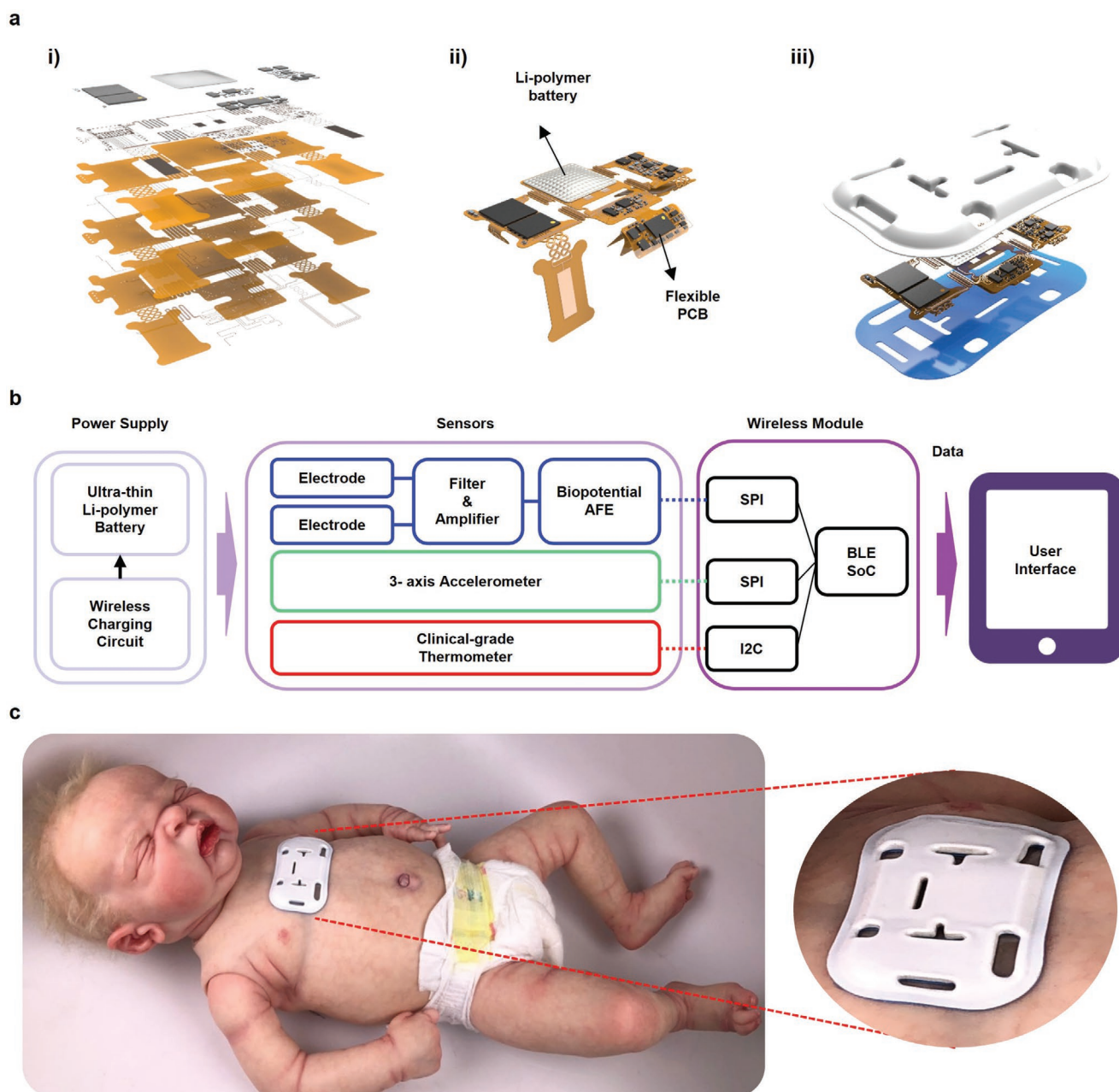


Figure 1. Schematic diagrams and images of a soft, holey wireless device for measuring electrocardiograms (ECGs) and skin temperature, and for capturing tri-axis accelerometry data. a) Exploded view illustration of a device with a rechargeable battery. The four-layer flexible printed circuit board supports circuit components on island structures, with serpentine filamentary interconnects configured for a folding process conducted prior to encapsulation. Precompression of these interconnects increases the elastic stretchability of the system. Openings formed through the elastomeric encapsulation structure provide key advantages in mechanics, adhesion release, visual inspection, and breathability. b) Block diagram of the operational scheme of the device with analog-front-end for ECG processing, tri-axis accelerometer, thermometer IC, and BLE SoC. c) Images of a device on the chest of a realistic model of a neonate.

2. Results and Discussions

2.1. Thin, Soft, Holey Platform for Wireless Health Monitoring in the NICU/PICU

Figure 1a presents schematic illustrations of a thin, soft wireless device with a holey architecture of the type described above.

The electronics consist of a flexible printed circuit board (fPCB; total thickness 173 μm) that includes four layers of copper (Cu) and five layers of polyimide (PI) structured to include thin, narrow serpentine conductive traces (widths between 76 and 375 μm wide; thickness 12 μm) that interconnect a collection of chip-scale integrated components (lateral dimensions between 1 mm^2 and 64 mm^2 ; thicknesses between 0.5 and 1.5 mm). The

thicknesses (12 μm) and widths (75 μm) of the Cu traces align with those that can be achieved in typical fPCB manufacturing. A small, rechargeable lithium-polymer battery (DNK201515; $15 \times 15 \text{ mm}^2$; thickness 2 mm) supplies power for operation. As described in detail in subsequent sections, holes formed through the fPCB and the encapsulation structure reduce the effective modulus and bending rigidity to facilitate gentle application and removal from the skin. Additional enhancements include layouts with predefined, molded curvature designed to match that of a targeted body location. The system supports wireless monitoring of the full range of vital signs and other parameters described in the Introduction, using Bluetooth protocols to allow the use of a standard smartphone as the graphical user interface and location for data storage and processing.

As shown in Figure 1b, these functions follow from an associated collection of sensors that includes an inertial measurement unit (LSM6DSL, STMicroelectronics), a clinical-grade temperature gauge (MAX30205, Maxim Integrated), and a subsystem for recording electrocardiograms (ECGs) through two gold-plated electrodes and a biopotential analog front-end (MAX30001, Maxim Integrated). A Bluetooth Low Energy (BLE) system-on-a-chip (SoC) supports wireless transfer of data acquired from these sensors for real-time display on a tablet computer and/or for storage on a memory module including in the device itself (MT29F2G01ABAGDWB, Micron Technology Inc.). The battery has a storage capacity of 20 mAh, sufficient to support operation for 24 h before requiring a recharge. A power management circuit includes a regulator to convert the voltage (3.7 V) of the battery to the voltage (3.3 or 1.8 V) necessary for the components of the device. A wireless circuit uses an induction coil for charging the battery.

The assembly and encapsulation process begins with folding of the fPCB islands at hinge points defined by serpentine interconnects, to reduce the overall size of the device (Figure 1a, middle; and Figure S1, Supporting Information). The serpentine include four Cu layers, precompressed by 30% to enhance their flexibility and stretchability (Figures S2 and S3, Supporting Information). FEA results indicate that the strain in each Cu layer remains below the fracture limit ($\approx 1\%$) throughout these steps (Figures S2–S4, Supporting Information). After this assembly process, the serpentine interconnects can stretch along their length by up to 85% without inducing fractures in the Cu (Figure S5, Supporting Information). The top and bottom layers of the encapsulation structure consist of a low modulus silicone material (5 MPa; Silbione RTV 4420) molded into the desired shapes. A silicone polymer with a different formulation (0.069 MPa; Ecoflex 00-30) injected in between these layers fills the empty spaces in a manner that maintains the softness of the overall platform and minimizes mechanical constraints on motions of the serpentine interconnects induced by bending or stretching. The maximum stretching that the devices can accommodate before fracture of the Cu serpentine traces is 85%. This material also prevents damage of the encapsulation layer by the rigid electronic components and entanglement of the serpentine interconnects (Figure 1a, right; and Figure S6, Supporting Information).^[28] The photograph in Figure 1c shows a device with this construction mounted on the curved chest of a realistic neonate model, bonded to the surface with a hydrogel adhesive (KM 40A hydrogel,

Katecho Inc.; thickness $\approx 815 \mu\text{m}$). The hydrogel layer is thin, flexible, and stretchable, which allows for gentle placement of the device on the curved skin of the chest; electrical conductivity allows recording of ECG data.^[17,19] After use for 24 h of device operation, there is no significant change in the weight of the hydrogel adhesive, suggesting the potential for long-term application (Figure S24, Supporting Information).^[29,30] Also, the heat generated by the working device is negligible (Figure S25 Supporting Information).

2.2. Mechanical Characteristics Associated with Holey Designs

Some holes reside near the serpentine interconnects to preserve their high flexibility and stretchability; others lie inside the center island to facilitate deformations in this part of the device. Holes of various shapes near the border area promote low stiffness and modulus at locations where peeling initiates, to reduce skin irritation during device application and removal. This holey design maximizes their overall area, limited by space available as dictated by the electronics layouts. Systematic studies by FEA define various advantages of this layout in effective modulus and bending stiffness, as well as in corresponding degrees of stretchability and bendability. The photographs in Figure 2a show the device bent along its long axis to a radius of 22 mm (left) and along the orthogonal direction to a radius of 5.3 mm (middle) and through a twisting angle of 125° (right). The three main islands that support the IC chips and the battery include stiffeners of rigid printed circuit board material (Garolite G-10/FR-4, thickness 381 μm). These elements effectively eliminate bending in these areas, to avoid possible damage to the solder joints between the components and the fPCB. The islands support the active components; the serpentine interconnects enable mechanical deformations. All system level deformations of the device involve motions of the serpentine interconnects, such that strains in the Cu ultimately limit the range of stretchability and bendability. The maximum principal strains in the Cu layers remain below the yield strain of 0.3% (Figure 2b; and Figures S7–S9, Supporting Information), for the cases examined here. During device application and removal, skin irritations can result from interface stresses and associated deformations at the surface of the skin. Comparisons of deformations associated with devices that use holey and nonholey designs yield insights into the relative potential for inducing skin irritation in these two cases. Comparisons to standard (i.e., nonholey) devices with otherwise similar designs reveal that the presence of the holes reduces the strains across all functional materials by 34.4% (bending), 28.8% (orthogonal bending), 15.5% (twisting), 14.1% (stretching) for these cases (Figure 2c; and Figure S10, and Table S1, Supporting Information). Similar comparisons indicate that the holes decrease the stiffness and modulus by $\approx 30\%$ for parallel/horizontal bending, $\approx 23\%$ for twisting and $\approx 20\%$ for uniaxial stretching (Figure 2d; and Figure S11, Supporting Information). These features also lead to stresses at the interface with the skin that remain below thresholds for sensory perception for adults (20 kPa) for uniaxial stretching of up to 20%, a value at the high end of the range expected in practical use (Figure S12, Supporting Information).^[31–34]

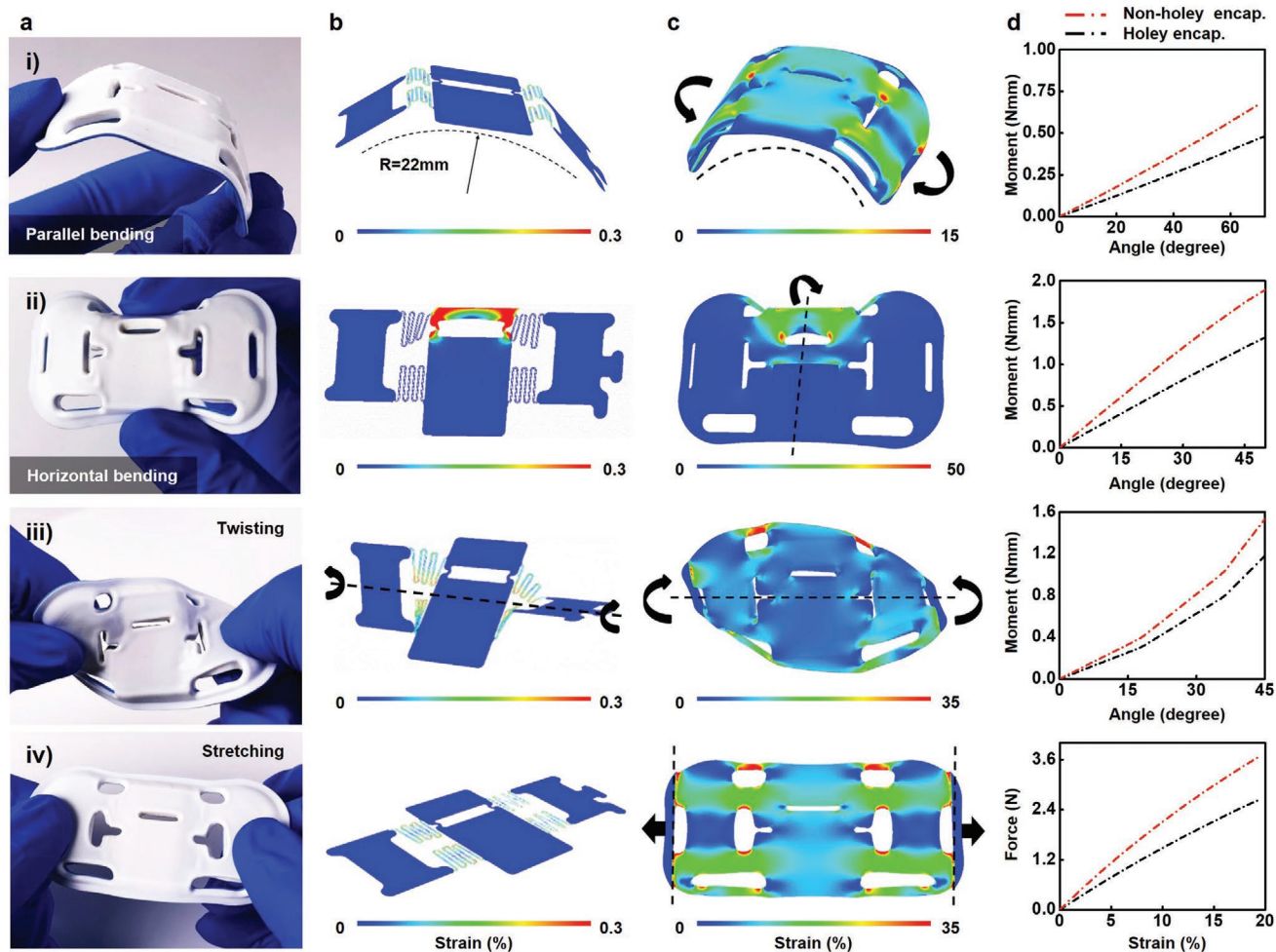


Figure 2. Mechanical characterization results and images of a soft, holey, wireless vital signs monitoring device under various mechanical deformations. a) Images of a representative device during i) parallel bending, ii) horizontal bending, iii) twisting, and iv) stretching. b) Simulation results for the deformed geometries and strain distributions in the copper layer of the electronic system. c) Simulation results for the deformed geometries and strain distributions in entire encapsulated device during corresponding deformations. d) Comparisons of moment-angle and force-strain responses for holey and nonhole device designs.

2.3. Mechanical Characteristics Associated with Curved Designs

Devices with predefined curvature further improve the mechanics at the skin interface. Applying conventional planar devices onto the surfaces of the body requires bending. The associated bending-induced stresses can promote delamination in certain cases and they can cause skin irritation in others. Both effects are pronounced for premature neonates due to their small, highly curved anatomical features and their fragile skin.^[22,35,36] The mitigation strategy introduced here exploits encapsulation layers formed in curved geometries approximately matched to those of the desired mounting location and size/age of the baby. **Figure 3a** shows devices with planar and with curved shapes. The examples here involve bending radii (angle) of 108 mm (30°) and 54 mm (60°) matched to the chest circumference of pediatric patients (11–12 ages: ≈65–70 cm)^[37] and newborns (30–35 cm).^[38] When attaching the device to the surfaces of skin with different curvatures (planar, 30° curved, 60° curved), mismatch with the curvature of device results

in a resilience associated with elastic forces directed toward returning the bent device to its original shape. The stresses caused by this resilience appear most prominently near the islands of the device due to their large stiffnesses compared to those of the encapsulation structures (Figure 3b–d). For the planar device (Figure 3b), the maximum stress is –15 kPa (compression) and 15 kPa (tension), –28 kPa (compression) and 38 kPa (tension) for cases of 30° and 60° mismatch in curvature, respectively. For the cases of devices with precurvatures of 30° (Figure 3c), the maximum stresses are –12 kPa (compression) and 7 kPa (tension) for a curvature mismatch of 30°. All cases where the curvatures are matched (=0° mismatch) exhibit zero stress. Figure S14 (Supporting Information) shows the calculations of stress distributions for such devices mounted on skin with matching curvature and tangentially stretched to 15%. The interfacial stresses are below the somatosensory pressure range (20 kPa) of the skin even when the skin is stretched by 15%.^[39] These results of FEA show that the precurved encapsulation approach reduces the stress to the skin. These effects

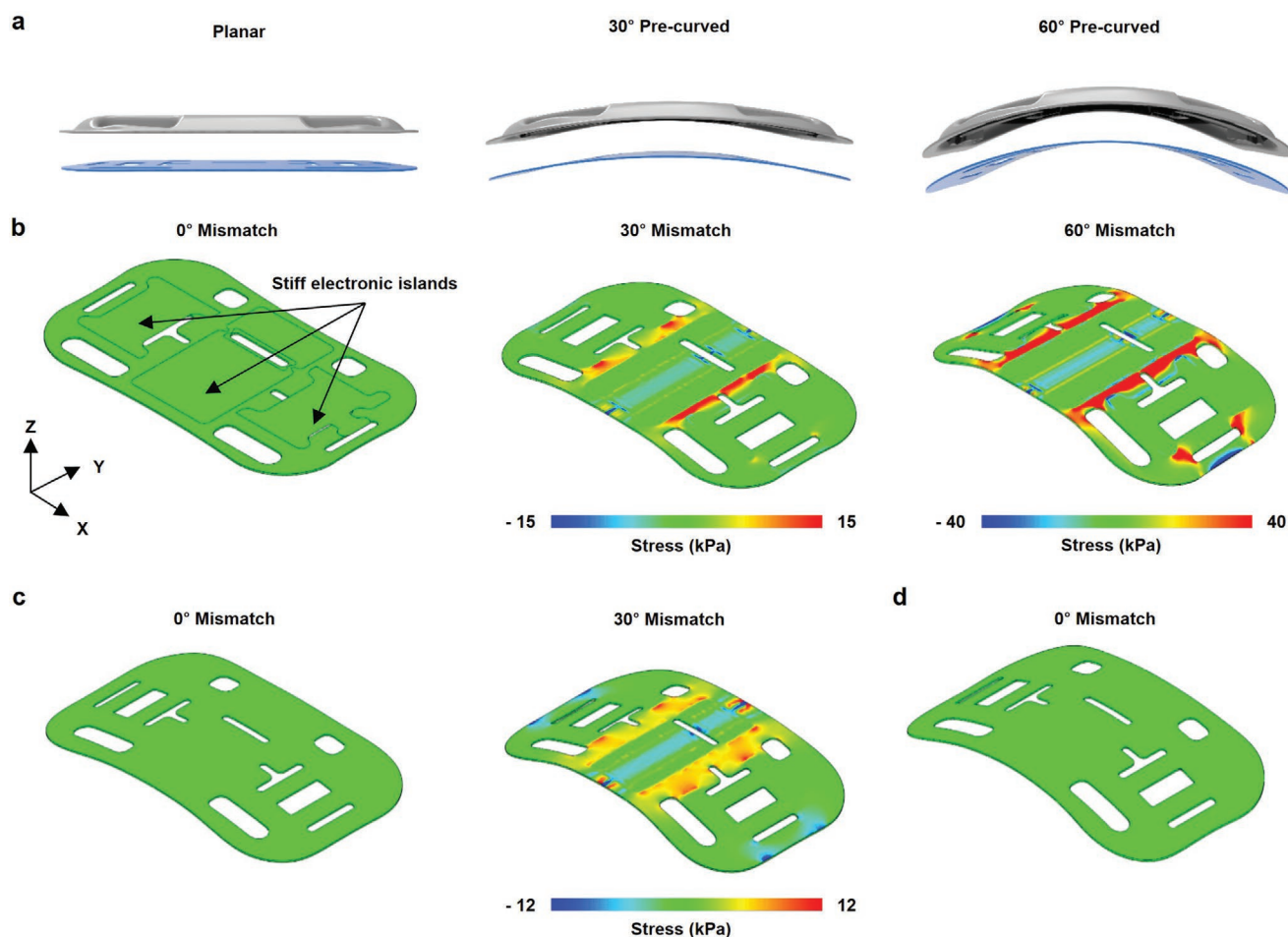


Figure 3. Precurved holey ECG devices with different curvatures. a) Images of (left) planar, (middle) 30° and (right) 60° precurved designs. Comparison of computed stresses induced by the resilience from curvature mismatch between the skin and the device. b) The planar device for 0°, 30°, and 60° mismatch. c) The 30° precurved device for 30° mismatch. d) The 60° precurved device for 0° mismatch.

minimize mechanically induced irritation to the skin and they promote robust interfaces.

2.4. Water-Triggered Reduction of the Strength of Adhesion to the Skin

As described previously, the process of removing devices from the skin can cause iatrogenic injuries. Thin, soft and wireless devices significantly reduce the strength of adhesion necessary to support robust bonding compared to that required for conventional wired sensors.^[18] Nevertheless, separate, triggering mechanisms to reduce the adhesion to facilitate release can be valuable. In a strategy introduced here, water applied to the holes and the surrounding perimeter of the device cause swelling of a hydrogel bonding layer, thereby reducing the strength of adhesion dramatically, even to levels that can be considered negligible.^[23–25] The hydrogel adhesive is based on 2-acrylamido-2-methylpropane sulfonic acid/acrylic acid (AMPS/AA) copolymer.^[16] Water reduces the adhesion by hydrating and decomposing the hydrogel network.^[40] After immersion for 24 h, the hydrogel is fully decomposed

(Figure S23, Supporting Information). Figure 4a shows the basic effect, measured as peel force required to remove a rectangular hydrogel adhesive (10 × 30 mm², thickness Supporting Information 815 μm) attached to a glass slide (Figure S15, Supporting Information), as a function of time of immersion in water at temperatures of 25 and 35 °C.^[41,42] The diffusion coefficient for water through the hydrogel (≈1.2 mm² min⁻¹) at 35 °C is approximately twice as large as that (≈0.6 mm² min⁻¹) at 25 °C, thereby resulting in a correspondingly higher swelling rate and a more rapid reduction in peel force (Figure S16, Supporting Information).^[43–45] Complete loss of adhesion, to within measurement uncertainties, occurs in 7 and 11 min at 35 and 25 °C, respectively. The 35 °C case, close to the temperature of the skin, is most relevant for applications considered here.

Without holes, this release mechanism is not practical because water can be introduced only around the perimeter of the device. The hydrogel adhesive consists of two separate pieces, one for each of the ECG electrodes. The widths of each piece are equal to half of that of the entire device. As such, the minimum diffusion distance is equal to one quarter of the width of the device (≈13.6 mm) for complete wetting of the hydrogel. The holes represent additional points of access that also

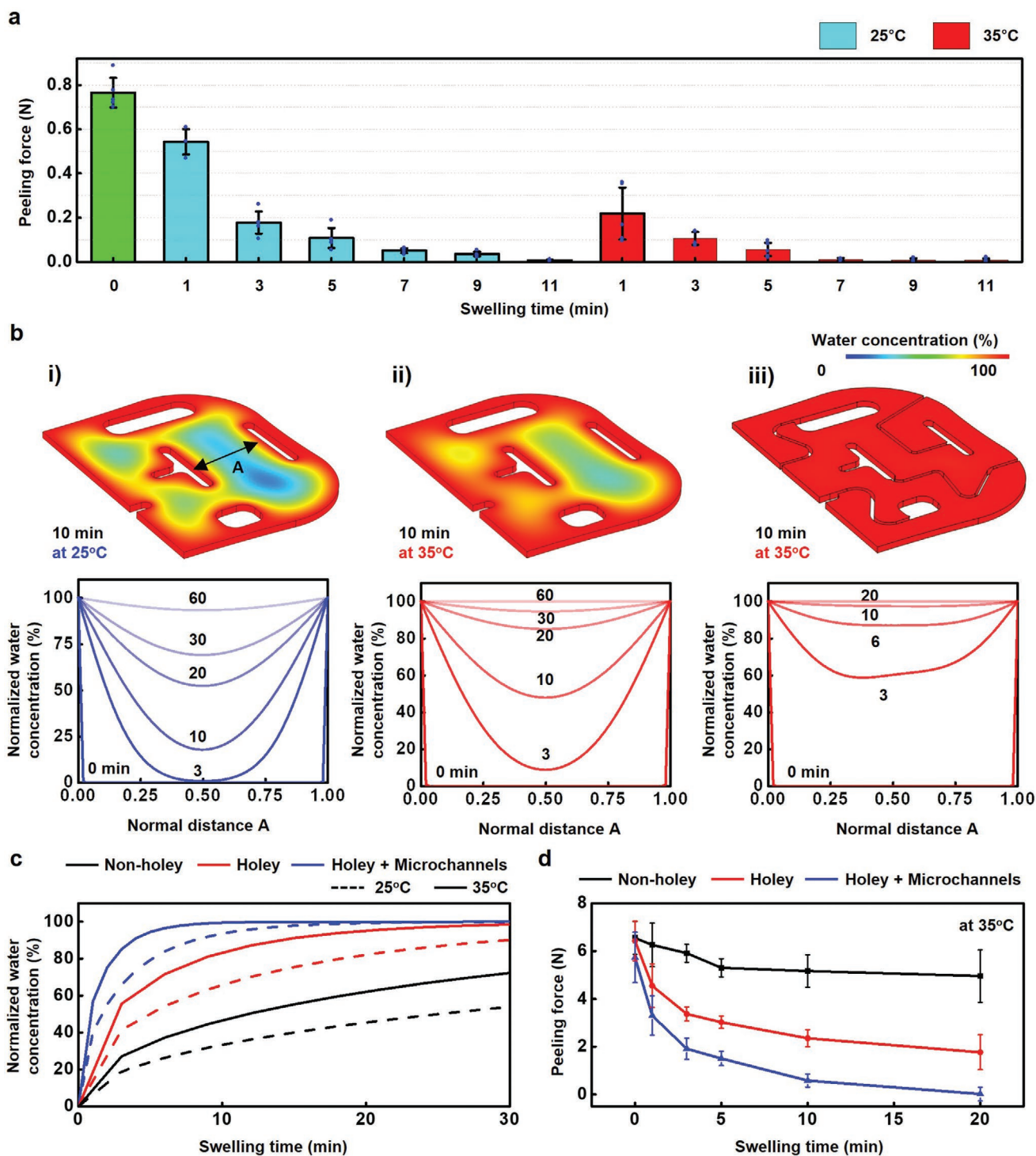


Figure 4. Water triggered soft release of the hydrogel adhesive. a) Peel force of hydrogel adhesive as a function of swelling time and water temperature (25 and 35 °C). b) Computed swelling model of the hydrogel adhesive during water diffusion through the holey device and the difference in water concentration of the hydrogel adhesive as a function of swelling time, water temperature, and adhesive design; i) holey design at 25 °C, ii) holey design at 35 °C, and iii) holey design with microchannels at 35 °C. c) Comparison of water concentration averaged across the entire volumes of these different designs, at these two temperatures. d) Comparison of peeling force as a function of swelling time for hydrogel adhesives with different designs: non-holey, holey, and holey with microchannels for water at 35 °C.

simultaneously act as reservoirs, to reduce this distance. For the configuration of holes examined here, this reduction

corresponds to a factor of ≈ 2 (≈ 6.7 mm). Given the quadratic dependence of diffusion distance on time in Figure S17

(Supporting Information),^[43] this reduction translates to a decrease in the time to achieve saturation by a factor of ≈ 4 . To reduce further the minimum diffusion distance and saturation time, the holes can serve as the origins for features that facilitate lateral transport (Figure S18, Supporting Information). Here, water introduced into the holes flows through microchannels (width: 500 μm , thickness: thickness 812.8 μm) cut into the hydrogel itself (Figure S19 and Video S1, Supporting Information). Each hole acts as an inlet, with outlets formed on the outermost part of the hydrogel adhesive so that water injected through the holes can flow through the microchannels without backpressure. The microchannels were designed to pass through the areas where water does not pass due to simple diffusion after 10 min of swelling in the hydrogel adhesive (Figure 4b; and Figure S20, Supporting Information). These features further reduce the minimum diffusion distance (to ≈ 3 mm), corresponding to a reduction of saturation time by another factor of more than four (≈ 4.4 times) and by nearly 20 times compared to that of a conventional design, without holes or microchannels. Figure 4b,c; and Figure S20 (Supporting Information), shows simulation results that use measured diffusion coefficients of hydrogel adhesive for water at 25 and 35 $^{\circ}\text{C}$ to compare these various cases (nonholey, holey, and holey with microchannels). The hydrogel adhesive has an initial water content of 23%, as a baseline for calculating the normalized water concentration due to diffusion. Results of FEA capture the diffusion of water over the swelling time for each design of the hydrogel adhesive, as changes in the normalized water concentration with distance (line marked A in Figure 4b) and through the entire volume (Figure 4c). In the holey design, the center point of this line reaches a normalized water concentration of $\approx 20\%$ and 50% at 10 min for temperatures of 25 and 35 $^{\circ}\text{C}$, respectively. For the holey design with microchannels, the concentration reaches 90% at 10 min for 35 $^{\circ}\text{C}$. Table S2 (Supporting Information) shows the calculated saturation times for these three designs at 25 and 35 $^{\circ}\text{C}$. The holey design with microchannels at 35 $^{\circ}\text{C}$ exhibits a saturation time that is ≈ 27.5 times (8 min) smaller than that (220 min) of the nonholey case at 25 $^{\circ}\text{C}$.

Experimental measurements of peeling force for devices adhered to the back of the hand of an adult volunteer subject show trends consistent with modeling (Figure 4c,d). Initially, all designs (nonholey, holey, and holey with microchannels) have peeling forces in the range of 5–7 N. Even after immersion in water at 35 $^{\circ}\text{C}$ for 10 min, the peeling force of the nonholey device shows the smallest reduction, still larger than 5.0 N, and the peeling force of the holey example is about 2.0 N. At that time, the peeling force of the holey with microchannels decreases by the largest amount, to a value less than 0.6 N. After 20 min, the device with holey design and microchannels exhibits zero adhesion, to within experimental uncertainties.

2.5. Moisture Release and Visual Inspection

Just as the holes and microchannels facilitate permeation of water to the device-skin interface to trigger release of adhesion, permeation of moisture away from this interface via similar mechanisms can avoid the development of a moist environment in which fungi and bacteria can reproduce and

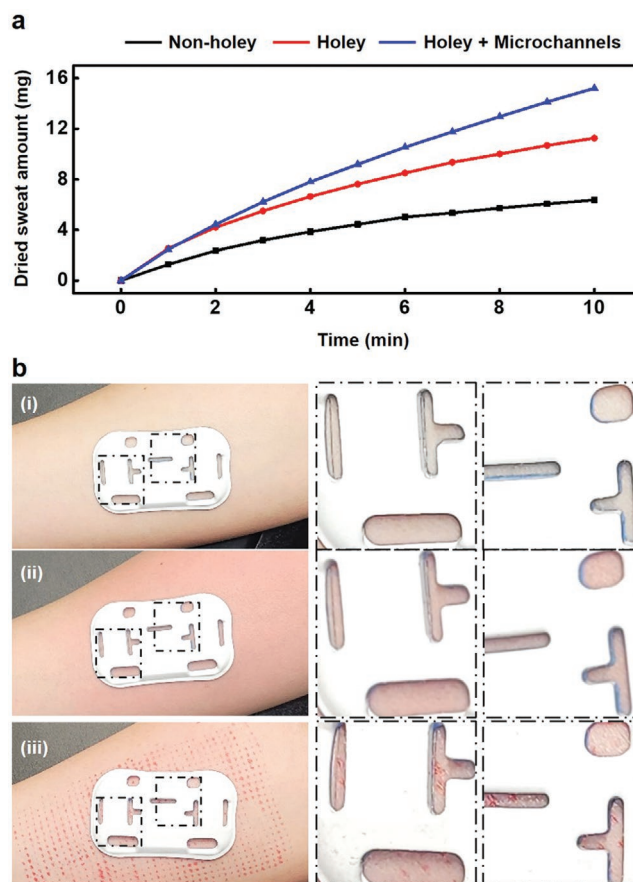


Figure 5. Measurements of breathability and demonstrations of visual inspection through the openings in a holey device. a) Comparison of the weight of water lost by evaporation from a saturated hydrogel that lies between the base of a device and a glass slide substrate, as a function of time for devices with nonholey, holey, and holey with microchannels designs. b) Images of devices with holey designs on i) normal skin, ii) skin reddened by irritation, iii) skin with artificial red spots imitating allergic reaction for visual inspection of skin condition through holes.

cause allergic dermatitis.^[26,27] The results in Figure 5a summarizes measurements of that involve placing a device on top of a sample of fully hydrated hydrogel bonded to a glass slide and measuring the amount of weight of water lost by evaporation as a function of time (Figure S22, Supporting Information). For the nonholey device, evaporation can only occur at the perimeter. For the holey device, evaporation occurs not only at the perimeter but also at the regions of the holes. The holey device with microchannels provides additional paths for water vapor to escape from the hydrogel. The findings suggest that the holey device offers breathability, as measured in this way, that is nearly two times (1.87) higher than the nonholey case. The enhancement for the holey device with microchannels corresponds to a factor of ≈ 2.4 . Also, the enhanced breathability of the holey device can prevent the swelling of hydrogel adhesive due to natural epidermal water loss and/or sweat.

The holes also provide visual access for inspecting the condition of the skin, without removing the device. Figure 5b shows pictures of holey devices on i) normal skin, ii) skin reddened by irritation, and iii) skin with artificial red spots to mimic allergic

reactions. The changes in skin color are immediately apparent through the holes. This feature enables early diagnosis of the occurrence of rash or dermatitis of the skin interface.

2.6. Operation in Capturing Electrocardiograms and High Bandwidth Accelerometry Data

The device described here supports single lead measurements of ECGs, tri-axis accelerations, and skin temperature. Data from the accelerometer yields SCGs, cycles of respiration (for determinations of RR), along with unique biomarkers derived from vibratory motions associated with crying and with coughing and wheezing, all without little effect of ambient sounds. **Figure 6a** shows representative ECGs, SCGs, and results of RR captured from adult volunteer subjects with a holey device attached to their chests. The raw data continuously passes wirelessly to a mobile tablet that supports data analysis through a signal processing algorithm, for real-time graphical display.^[19] **Figure 6b** shows 20 min of HR data compared to that collected with a clinical standard monitor (Intellivue MP50, Philips) in the intensive care unit. **Figure 6c–e** presents quantitative comparisons of HR, RR, and temperature for three adult volunteer subjects using the Bland–Altman method.^[46] The mean difference and standard deviation (s.d.) are 0.64 and 1.69 beats per minute, -2.72 and 2.81 breaths per minute, and -0.74 and 0.27 °C, respectively. The results for HR and RR are within ± 5 beats per minute and ± 3 breaths per minute, both compatible with regulatory guidelines set by the US FDA. The accelerometer also provides clinically important information on body motions/movements and orientation, along with vocal biomarkers and body sounds mentioned previously.^[20,21] **Figure 6f** shows accelerometer data from adult volunteer subject under various situations such as sitting, coughing, laughing, low/normal/high talk, and walking.

2.7. Clinical Studies on a Neonatal Patient in the NICU

Figure 7a,b is the planar holey ECG device and the 60° pre-curved holey ECG device on the newborns, respectively. **Figure 7c** shows the holey ECG device on a neonatal patient. The neonatal patient (male, weight 2.56 kg, height 47 cm) is 38 weeks postmenstrual ages (36 weeks gestational age + 2 weeks chronological age) with diagnoses of prematurity and respiratory distress of newborn. In **Figure 7c**, the left photograph shows the holey ECG device attached to a chest of this patient using the hydrogel adhesive, the middle photograph shows the process of introducing the saline through holes for the water-triggered soft release of hydrogel adhesive after monitoring for 1 h, and the right photograph shows the skin condition after removal of the device and the hydrogel adhesive. Although the part where the device is attached is slightly depressed, the device and the adhesive can be gently and easily removed without damaging the fragile skin. **Figure 7d** shows representative ECGs, SCGs captured the device attached to the chest, and **Figure 7e** shows 1 h of HR data compared to that collected with a gold standard system. **Figure 7f** presents quantitative comparisons of HR for the neonatal patient using the

Bland–Altman method.^[46] The mean difference and s.d. are -0.5 and 5.79 , respectively, showing compatibility with guidelines set by the US FDA.

3. Conclusion

This paper introduces materials and design concepts for thin, soft wireless devices that can continuously monitor key vital signs, such as HR, RR, and temperature, and body motion/movements, with a focus on patients in the NICU and PICU. Key features include holey architectures, precurved layouts and structured hydrogel adhesives. The locations, dimensions, and shapes of the holes improve the bending and stretching mechanics, to reduce irritation at the skin interface during device application, use, and removal. Further increases in the flexibility and stretchability of the devices can be achieved by use of a larger number of smaller islands in the fPCB, each connected with serpentine in layouts that create spaces for holes. Multilayer, folded fPCB designs can facilitate this scaling. Precurved shapes that match those of the targeted region of the anatomy further decrease the stresses on the surface of the skin, to values close to zero. In addition to these mechanical and geometrical advantages, the holey designs enable i) soft release of devices from the skin triggered by introduction of warm water through the holes and into microchannels molded on thin, hydrogel skin adhesives, ii) reduced accumulation of interfacial moisture from transepidermal water loss via enhanced rates of permeation through the holes, iii) visual inspection of the skin condition in the regions of the holes, without the need to remove the devices. Studies with adult volunteer subjects demonstrate the ability to capture HR, RR, and skin temperature with high levels of reliability and accuracy, along with measurements of body motions/movements. A clinical demonstration with a neonatal patient in an operating NICU shows that HR data from a holey device compare quantitatively to those collected using clinical standard apparatus and that the water-triggered soft release mechanism can be exploited in a commercial grade isolette, without significant change to routine procedures used with such patients. The outcomes of this work have the potential to enhance the quality of care for the neonates in all contexts, from the most advanced hospital settings to rural or remote health clinics in resource-constrained areas.

4. Experimental Section

Fabrication and Encapsulation of the Holey Device: A ISO 9001-compliant PCB manufacturer provided the fPCB for the holey device based on designs formed using Eagle CAD version 9 (Autodesk). Assembling components and programming the chips completed the functional electronics. The device includes passive components (resistors, inductors, and capacitors; footprint in inch from 0201 to 0603), power-management units (BQ25120A, Texas Instrument; TPS7A25, Texas Instrument), a BLE SoC (ISP1807-LR, Insight SIP), an ECG sensing unit (MAX30001, Maxim Integrated), an inertial measurement unit (LSM6DSL, STMicroelectronics), and a thermometer unit (MAX30205, Maxim Integrated). A folding process reduced the overall size of the device. A thin polyorganosiloxane elastomer film (Silbione RTV 4420, Elkem, mixed with 5 wt% blue silicone dye (Silc-Pig, Smooth-On)) formed by spin-casting at 250 rpm on a glass slide and thermal curing

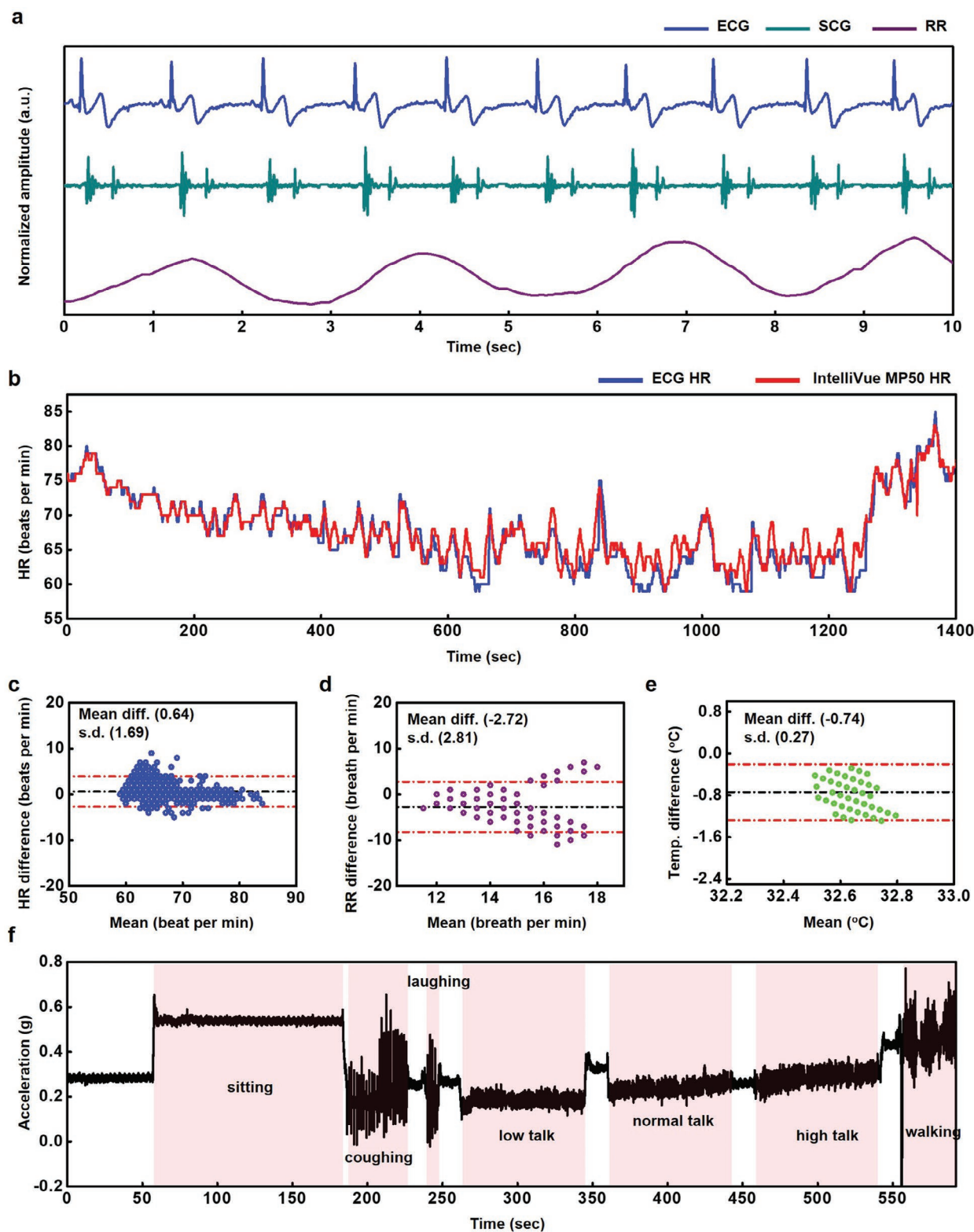


Figure 6. Representative data collected from a holey device. a) Representative ECG, SCG and respiration (RR) wave forms. b) Comparison of HR, RR and temperature to standard clinical measurements. c–e) Corresponding Bland–Altman plots for c) HR, d) RR, and e) temperature. f) Data captured from the accelerometer for various scenarios, including sitting, coughing, laughing, soft talking, normal talking, loud talking, and walking.

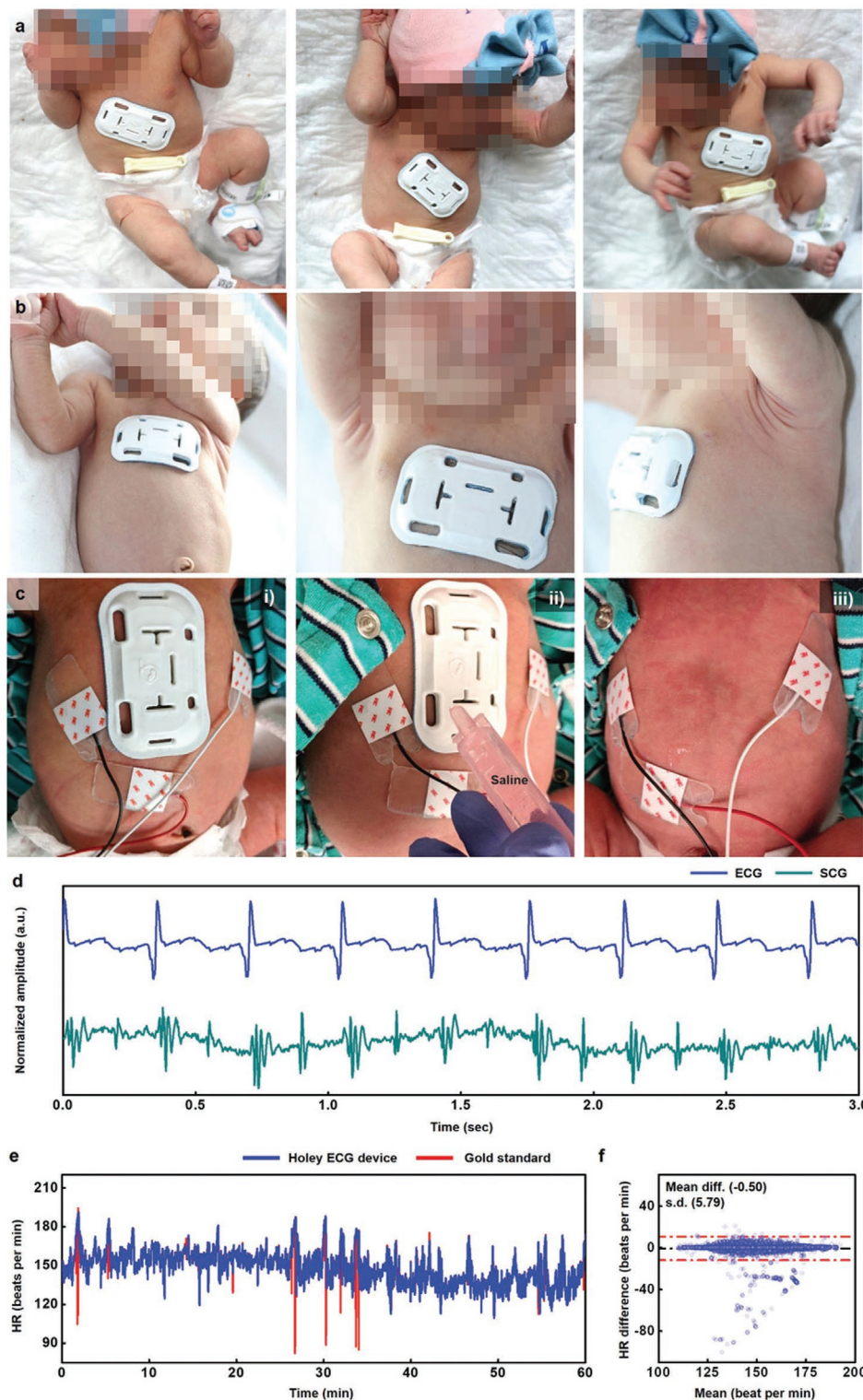


Figure 7. Clinical demonstrations of a holey device with the newborns and a neonatal patient in an operating NICU. a) Representative photographs of the planar holey device on the newborns. b) Representative photographs of the 60° precurved holey device on the newborns. c) Representative photographs of the holey device on a preterm infant (male, weight 2.56 kg, height 47 cm) of 38 weeks post menstrual age (36 weeks gestational age, 2 weeks chronological age) with diagnoses of prematurity and respiratory distress; i) when monitoring vital signs after mounting the device on the chest, ii) when applying saline through the holes to facilitate release of the hydrogel adhesive, iii) after the water-triggered soft release of the adhesive. The photos in (a), (b), and (c) appear with parental consent. d) Representative ECG, and SCG waveforms recorded from the patient using this device. e) Comparison of HR determined with the device and with a gold standard system. f) Corresponding Bland–Altman plot for HR.

at 100 °C for 20 min. served as a bottom encapsulation layer. A cutting process with a CO₂ laser (ULS) defined two openings for the ECG electrodes and eight openings with different shapes for the holey design on the bottom layer. A silicone-based adhesive (3M 96042) attached the folded electronics to the bottom layer. A pair of convex (with holes) and concave (with pillars) aluminum molds for the top encapsulation layer of holey device was designed using SOLIDWORKS 2019 (Dassault Systemes), and printed using a milling machine (MDX-540, Rolland DGA). A thin (≈300 μm) polyorganosiloxane elastomer film (Silbione RTV 4420, mixed with 5 wt% white silicone dye) formed using these molds and thermal curing at 100 °C for 20 min defined the top layer. The top layer and the bottom layer with the electronics were overlaid, and the enclosed device was filled with an uncured polyorganosiloxane elastomer (Ecoflex 00-30, Smooth-On) to improve the softness and prevent tearing of the top and bottom layer by the fPCB, component chips and battery during mechanical deformations, such as bending and twisting. The completely enclosed device was thermally cured at 80 °C for 20 min and the edges of encapsulation layer were cut to complete the encapsulation process.

Mechanical Simulation of the Device: ABAQUS, a commercial finite element analysis (FEA) software, was used to model the mechanical behavior of the serpentine interconnects used for the electronics and the different encapsulation designs when subjected to different types of deformation (stretching, bending, and twisting). The objectives of the analysis were to 1) assess possibilities for plastic deformation (i.e., $\epsilon < 0.3\%$) occurs in the copper serpentine interconnects when the device undergoes different types of external loads, 2) guide designs to reduce the magnitude of the strain in the optimized holey encapsulation, and 3) determine whether the interfacial normal and shear stresses imposed by the device onto the skin during deformation remain below the low somatosensory perception of the device on the skin for wearability, and 4) compare the resilience of the flat and precurved soft encapsulation designs associated with mounting on the curved surface of the skin. The thin copper (≈12 μm thick) and PI (≈25 μm thick) layers were modeled by composite shell elements (S4R), the soft encapsulation designs (with and without holes) were modeled by tetrahedron elements (C3D10), and the skin was modeled by hexahedron elements (C3D8R). The element size was tested to ensure convergence and accuracy of the simulation results. The elastic modulus (E) and Poisson's ratio (ν) were $E_{PI} = 2.5$ GPa and $\nu_{PI} = 0.34$ for PI; $E_{Cu} = 119$ GPa and $\nu_{Cu} = 0.34$ for copper; $E_{Silbione} = 0.8$ MPa and $\nu_{Silbione} = 0.5$ for Silbione; $E_{Ecoflex} = 60$ kPa and $\nu_{Ecoflex} = 0.5$ for Ecoflex; and $E_{Skin} = 130$ kPa and $\nu_{Skin} = 0.5$ for the skin.

Peeling Force Measurements of Hydrogel Adhesive on Slide Glass: Using the CO₂ laser (ULS), the hydrogel adhesive (KM 40A, Katecho) was cut into strips of 10 × 30 mm², and then adhered to the slide glass. A solid analyzer (RSA G2, Tainstruments) determined the peeling force associated with detachment of the hydrogel adhesive from the surface of a slide glass. The upper mount of the analyzer held one edge of hydrogel adhesive strip, and the slide glass was fixed to the lower mount. The upper mount moved at 0.3 mm s⁻¹ with the lower mount fixed, as the peeling force was recorded over time until the hydrogel adhesive strip was completely removed from the slide glass.

Diffusion Coefficient of Hydrogel Adhesive: The hydrogel adhesive strip (10 × 30 mm²) was immersed in water at 25 and 35 °C, and the change in weight of the hydrogel adhesive strip was recorded over time. The diffusion coefficient was determined to be 5.56 × 10⁻⁷ m² min⁻¹ for water at 25 °C and 1.18 × 10⁻⁶ m² min⁻¹ for water at 35 °C from nonlinear fitting of the following equation

$$C_t/C_\infty = 1 - \exp\left[-7.3(D * t/Z^2)^{0.75}\right] \quad (1)$$

to experimental data, where C_t , C_∞ , D , t , Z are the water content in a hydrogel adhesive strip at immersing time in water, the maximum water content, diffusion coefficient of water, immersing time in water, and thickness of the hydrogel adhesive strip, respectively.^[43–45]

Water Diffusion Simulation in the Hydrogel: COMSOL, a commercial Multiphysics FEA software, was used to model the water concentration

as a function of time in the nonholey, holey, and holey + microchannels hydrogel adhesive layouts at 25 and 35 °C. The objective of the analysis was to determine the total diffusion time and to guide optimization of the holey + microchannel configuration for optimized rates of diffusion. The time-dependent diffusion was modeled according to

$$\frac{\partial c}{\partial t} + \nabla \cdot (-D\nabla c) = 0 \quad (2)$$

where, D is the diffusion coefficient (m² min⁻¹), c is the water concentration (mol m⁻³), and t is time (min). The hydrogel (≈812.5 μm thick) was modeled using tetrahedral elements and the total number of elements in the model is ≈340 000. The diffusion model used in the simulation are determined from experiments as $D = 5.56 \times 10^{-7}$ m² min⁻¹ at 25 °C and $D = 1.18 \times 10^{-6}$ m² min⁻¹ at 35 °C.^[43]

Peeling Force Measurements of Hydrogel Adhesive on Skin: Three designs (nonholey, holey, and holey with microchannels) of the hydrogel adhesive (KM 40A) were adhered to the precleaned back of hand. A clamp held one edge of hydrogel adhesive, attached to a force gauge (Mark-10) with a motorized test stand (Mark-10) to measure the peeling force. The linear motor moved at 0.5 mm s⁻¹. The peeling force was recorded over time until the hydrogel adhesive was completely detached from the skin.

Water Evaporation Measurements of Hydrogel Adhesive: Three designs (nonholey, holey, and holey with microchannels) of the hydrogel adhesive (KM 40A) were adhered to the fully encapsulated holey device, and then immersed into water to allow the hydrogel adhesive to absorb the water. The unabsorbed water on the surface of hydrogel adhesive was removed with a paper wipe, and the device with the hydrogel adhesive was attached to a slide glass. At room temperature, water absorbed by the hydrogel adhesive evaporated and the resulting loss of weight was recorded over time.

Clinical Study Design: The feasibility of the wireless, holey chest sensor in a clinical setting was tested in a Level III NICU facility, under approved research protocols by the Institutional Review Boards of the Ann & Robert H. Lurie Children's Hospital of Chicago (IRB 2018-1668) and Northwestern University (STU00208150). After informed consent was obtained and proper sterilization of the device, according to approved procedures by the infection control committee of the Ann & Robert H. Lurie Children's Hospital of Chicago,^[19] the sensor was gently placed onto the chest of the patient and adhered to the skin with two pieces of hydrogel adhesive (KM40A, Katecho). An iPad Pro with custom software applications, situated by the patient's bedside, was wirelessly connected to the sensor, allowing for continuous data collection and storage. A software application (MediCollector BEDSIDE) system was utilized to extract ECG data from the existing standard-of-care patient bedside monitor (Intellivue MP70, Philips). A drop of saline solution (0.9 wt% NaCl, Modudose) was added through each hole of the sensor to enable swelling of the underlying hydrogel adhesive and to facilitate release of the device from the skin.

Supporting Information

Supporting Information is available from the Wiley Online Library or from the author.

Acknowledgements

S.S.K., S.Y., R.A., and H.U.C. contributed equally to this work. R.A. acknowledges support from the National Science Foundation Graduate Research Fellowship (NSF Grant No. 1842165) and Ford Foundation Predoctoral Fellowship. Z.X. acknowledges the support from the National Natural Science Foundation of China (Grant No. 12072057), Liaoning Revitalization Talents Program (Grant No. XLYC2007196), and Fundamental Research Funds for the Central Universities (Grant No. DUT20RC(3)032). This work was supported by the Querry-Simpson

Institute for Bioelectronics at Northwestern University and Dr. Xu recognizes support from a Hartwell Individual Biomedical Award.

Note: Figure 7 was reset and the caption revised on November 4, 2021, after initial publication online.

Conflict of Interest

The authors declare no conflict of interest.

Data Availability Statement

The data that support the findings of this study are available from the corresponding author upon reasonable request.

Keywords

electrocardiogram, neonates, pediatrics, physiological monitoring, soft electronics, wireless wearables

Received: May 25, 2021

Revised: July 28, 2021

Published online: September 12, 2021

- [1] D. S. Wheeler, H. R. Wong, *Pediatric Critical Care Medicine: Basic Science and Clinical Evidence*, Springer Science & Business Media, Berlin **2007**.
- [2] J. Xu, S. L. Murphy, K. D. Kochanek, B. Bastian, E. Arias, *Natl. Vital Stat. Rep.* **2018**, *67*, 1.
- [3] O. Bonner, K. Beardsall, N. Crilly, J. Lasenby, *BMJ Innov.* **2017**, *3*, 12.
- [4] P. H. T. Cartlidge, P. E. Fox, N. Rutter, *Early Hum. Dev.* **1990**, *21*, 1.
- [5] C. Lund, *Newborn Infant Nurs. Rev.* **2014**, *14*, 160.
- [6] A. C. Tottman, J. M. Alsweller, F. H. Bloomfield, J. E. Harding, *BMJ J.* **2018**, *103*, F277.
- [7] D.-H. Kim, N. Lu, R. Ma, Y.-S. Kim, R.-H. Kim, S. Wang, J. Wu, S. M. Won, H. Tao, A. Islam, K. J. Yu, T. Kim, R. Chowdhury, M. Ying, L. Xu, M. Li, H.-J. Chung, H. Keum, M. McCormick, P. Liu, Y.-W. Zhang, F. G. Omenetto, Y. Huang, T. Coleman, J. A. Rogers, *Science* **2011**, *333*, 838.
- [8] W. Gao, S. Emaminejad, H. Y. Y. Nyein, S. Challa, K. Chen, A. Peck, H. M. Fahad, H. Ota, H. Shiraki, D. Kiriya, D.-H. Lien, G. A. Brooks, R. W. Davis, A. Javey, *Nature* **2016**, *529*, 509.
- [9] J. A. Walsh, E. J. Topol, S. R. Steinhubl, *Circulation* **2014**, *130*, 573.
- [10] K.-I. Jang, K. Li, H. U. Chung, S. Xu, H. N. Jung, Y. Yang, J. W. Kwak, H. H. Jung, J. Song, C. Yang, A. Wang, Z. Liu, J. Y. Lee, B. H. Kim, J.-H. Kim, J. Lee, Y. Yu, B. J. Kim, H. Jang, K. J. Yu, J. Kim, J. W. Lee, J.-W. Jeong, Y. M. Song, Y. Huang, Y. Zhang, J. A. Rogers, *Nat. Commun.* **2017**, *8*, 15894.
- [11] S. Y. Heo, J. Kim, P. Gutruf, A. Banks, P. Wei, R. Pielak, G. Balooch, Y. Shi, H. Araki, D. Rollo, C. Gaede, M. Patel, J. W. Kwak, A. E. Peña-Alcántara, K.-T. Lee, Y. Yun, J. K. Robinson, S. Xu, J. A. Rogers, *Sci. Transl. Med.* **2018**, *10*, eaau1643.
- [12] Y. Park, K. Kwon, S. S. Kwak, D. S. Yang, J. W. Kwak, H. Luan, T. S. Chung, K. S. Chun, J. U. Kim, H. Jang, H. Ryu, H. Jeong, S. M. Won, Y. J. Kang, M. Zhang, D. Pontes, B. R. Kampmeier, S. H. Seo, J. Zhao, I. Jung, Y. Huang, S. Xu, J. A. Rogers, *Sci. Adv.* **2020**, *6*, eabe1655.
- [13] A. Y. Rwei, W. Lu, C. Wu, K. Human, E. Suen, D. Franklin, M. Fabiani, G. Gratton, Z. Xie, Y. Deng, S. S. Kwak, L. Li, C. Gu, A. Liu, C. M. Rand, T. M. Stewart, Y. Huang, D. E. Weese-Mayer, J. A. Rogers, *Proc. Natl. Acad. Sci. USA* **2020**, *117*, 31674.
- [14] J. L. Vogl, E. C. Dunne, C. Liu, A. Bradley, A. Rwei, E. K. Lonergan, B. S. Hopkins, S. S. Kwak, C. D. Simon, C. M. Rand, J. A. Rogers, D. E. Weese-Mayer, C. F. Garfield, *Dev. Psychobiol.* **2021**, *5*, 1521.
- [15] H. Jeong, J. Y. Lee, K. Lee, Y. J. Kang, J.-T. Kim, R. Avila, A. Tzavelis, J. Kim, H. Ryu, S. S. Kwak, J. U. Kim, A. Banks, H. Jang, J.-K. Chang, S. Li, C. K. Mummissetty, Y. Park, S. Nappi, K. S. Chun, Y. J. Lee, K. Kwon, X. Ni, H. U. Chung, H. Luan, J.-H. Kim, C. Wu, S. Xu, A. Banks, A. Jayaraman, Y. Huang, J. A. Rogers, *Sci. Adv.* **2021**, *7*, eabg3092.
- [16] C. Liu, J.-T. Kim, S. S. Kwak, A. Hourlier-Fargette, R. Avila, J. Vogl, A. Tzavelis, H. U. Chung, J. Y. Lee, D. H. Kim, D. Ryu, K. B. Fields, J. L. Ciatti, S. Li, M. Irie, A. Bradley, A. Shukla, J. Chavez, E. C. Dunne, S. S. Kim, J. Kim, J. B. Park, H. H. Jo, J. Kim, M. C. Johnson, J. W. Kwak, S. R. Madhvapathy, S. Xu, C. M. Rand, L. E. Marsillio, S. J. Hong, Y. Huang, D. E. Weese-Mayer, J. A. Rogers, *Adv. Healthcare Mater.* **2021**, 2100383, <https://doi.org/10.1002/adhm.202100383>.
- [17] H. Liu, M. Li, S. Liu, P. Jia, X. Guo, S. Feng, T. J. Lu, H. Yang, F. Li, F. Xu, *Mater. Horiz.* **2020**, *7*, 203.
- [18] H. U. Chung, B. H. Kim, J. Y. Lee, J. Lee, Z. Xie, E. M. Ibler, K. Lee, A. Banks, J. Y. Jeong, J. Kim, C. Ogle, D. Grande, Y. Yu, H. Jang, P. Assem, D. Ryu, J. W. Kwak, M. Namkoong, J. B. Park, Y. Lee, D. H. Kim, A. Ryu, J. Jeong, K. You, B. Ji, Z. Liu, Q. Huo, X. Feng, Y. Deng, Y. Xu, K.-I. Jang, J. Kim, Y. Zhang, R. Ghaffari, C. M. Rand, M. Schau, A. Hamvas, D. E. Weese-Mayer, Y. Huang, S. M. Lee, C. H. Lee, N. R. Shanbhag, A. S. Paller, S. Xu, J. A. Rogers, *Science* **2019**, *363*, eaau0780.
- [19] H. U. Chung, A. Y. Rwei, A. Hourlier-Fargette, S. Xu, K. Lee, E. C. Dunne, Z. Xie, C. Liu, A. Carlini, D. H. Kim, D. Ryu, E. Kulikova, J. Cao, I. C. Odland, K. B. Fields, B. Hopkins, A. Banks, C. Ogle, D. Grande, J. B. Park, J. Kim, M. Irie, H. Jang, J. Lee, Y. Park, J. Kim, H. H. Jo, H. Hahm, R. Avila, Y. Xu, M. Namkoong, J. W. Kwak, E. Suen, M. A. Paulus, R. J. Kim, B. V. Parsons, K. A. Human, S. S. Kim, M. Patel, W. Reuther, H. S. Kim, S. H. Lee, J. D. Leadle, Y. Yun, S. Rigali, T. Son, I. Jung, H. Arafa, V. R. Soundararajan, A. Ollech, A. Shukla, A. Bradley, M. Schau, C. M. Rand, L. E. Marsillio, Z. L. Harris, Y. Huang, A. Hamvas, A. S. Paller, D. E. Weese-Mayer, J. Y. Lee, J. A. Rogers, *Nat. Med.* **2020**, *26*, 418.
- [20] M. C. Mahoney, M. I. Cohen, *Pediatr. Phys. Ther.* **2005**, *17*, 194.
- [21] Y. Shinya, M. Kawai, F. Niwa, M. Imafuku, M. Myowa, *Front. Psychol.* **2017**, *8*, 2195.
- [22] M. Y. Hadush, A. H. Berhe, A. A. Medhanyie, *BMC Pediatr.* **2017**, *17*, 111.
- [23] C. W. Peak, J. J. Wilker, G. Schmidt, *Colloid Polym. Sci.* **2013**, *291*, 2031.
- [24] R. Michel, L. Poirier, Q. van Poelvoorde, J. Legagneux, M. Manassero, L. Corté, *Proc. Natl. Acad. Sci. USA* **2019**, *116*, 738.
- [25] X. Du, Y. Hou, L. Wu, S. Li, A. Yu, D. Kong, L. Wang, G. Niu, *J. Mater. Chem. B* **2020**, *8*, 5682.
- [26] A. Miyamoto, S. Lee, N. F. Cooray, S. Lee, M. Mori, N. Matsuhisa, H. Jin, L. Yoda, T. Yokota, A. Itoh, M. Sekino, H. Kawasaki, T. Ebihara, M. Amagai, T. Someya, *Nat. Nanotechnol.* **2017**, *12*, 907.
- [27] S. Yoon, M. Seok, M. Kim, Y.-H. Cho, *Sci. Rep.* **2021**, *11*, 938.
- [28] K. Lee, X. Ni, J. Y. Lee, H. Arafa, D. J. Pe, S. Xu, R. Avila, M. Irie, J. H. Lee, R. L. Easterlin, D. H. Kim, H. U. Chung, O. O. Olabisi, S. Getaneh, E. Chung, M. Hill, J. Bell, H. Jang, C. Liu, J. B. Park, J. Kim, S. B. Kim, S. Mehta, M. Pharr, A. Tzavelis, J. T. Reeder, I. Huang, Y. Deng, Z. Xie, C. R. Davies, Y. Huang, J. A. Rogers, *Nat. Biomed. Eng.* **2020**, *4*, 148.
- [29] Y. Ye, Y. Zhang, Y. Chen, X. Han, F. Jiang, *Adv. Funct. Mater.* **2020**, *30*, 2003430.
- [30] Y. Niu, H. Liu, R. He, M. Luo, M. Shu, F. Xu, *Small* **2021**, *17*, 2101151.
- [31] A. Kaneko, N. Asai, T. Kanda, *J. Hand Ther.* **2005**, *18*, 421.

- [32] S. Wang, M. Li, J. Wu, D.-H. Kim, N. Lu, Y. Su, Z. Kang, Y. Huang, J. A. Rogers, *J. Appl. Mech.* **2012**, *79*, 031022.
- [33] C. H. Lee, Y. Ma, K.-I. Jang, A. Banks, T. Pan, X. Feng, J. S. Kim, D. Kang, M. S. Raj, B. L. McGrane, B. Morey, X. Wang, R. Ghaffari, Y. Huang, J. A. Rogers, *Adv. Funct. Mater.* **2015**, *25*, 3698.
- [34] A. Koh, D. Kang, Y. Xue, S. Lee, R. M. Pielak, J. Kim, T. Hwang, S. Min, A. Banks, P. Bastien, M. C. Manco, L. Wang, K. R. Ammann, K.-I. Jang, P. Won, S. Han, R. Ghaffari, U. Paik, M. J. Slepian, G. Balooch, Y. Huang, J. A. Rogers, *Sci. Transl. Med.* **2016**, *8*, 366ra165.
- [35] D. L. August, K. New, R. A. Ray, Y. Kandasamy, *J. Neonatal Nurs.* **2018**, *24*, 173.
- [36] T. Oranges, V. Dini, M. Romanelli, *Adv. Wound Care* **2015**, *4*, 587.
- [37] S. Patil, S. Patil, P. Durgawale, *J. Datta. Meghe Inst. Med. Sci. Univ.* **2018**, *13*, 143.
- [38] I. G. Azevedo, N. S. O. Holanda, N. M. R. Arrais, R. T. G. Santos, A. G. F. Araujo, S. A. Pereira, *BMC Pediatr.* **2019**, *19*, 341.
- [39] Y. Zhang, R. C. Webb, H. Luo, Y. Xue, J. Kurniawan, N. H. Cho, S. Krishnan, Y. Li, Y. Huang, J. A. Rogers, *Adv. Healthcare Mater.* **2016**, *5*, 119.
- [40] H. Yi, S. H. Lee, M. Seong, M. K. Kwak, H. E. Jeong, *J. Mater. Chem. B* **2018**, *6*, 8064.
- [41] Y. M. Lee, S. H. Kim, C. S. Cho, *J. Appl. Polym. Sci.* **1996**, *62*, 301.
- [42] S. J. Kim, S. J. Park, S. I. Kim, *React. Funct. Polym.* **2003**, *55*, 53.
- [43] J. Crank, *The Mathematics of Diffusion*, 2nd ed., Oxford University Press, New York **1975**.
- [44] C.-H. Shen, G. S. Springer, *J. Compos. Mater.* **1976**, *10*, 2.
- [45] H. S. Jang, G.-G. Kim, S. H. Kang, Y. Kim, J. I. Yoo, S. Yoo, K.-K. Kim, C. Jung, H. C. Ko, *Adv. Mater.* **2018**, *30*, 1801256.
- [46] J. M. Bland, D. G. Altman, *Lancet* **1986**, *327*, 307.